High-Resolution and Dispersed Fluorescence Examination of Vibronic Bands of Tryptamine: Spectroscopic Signatures for L_a/L_b Mixing near a Conical Intersection

Marcel Böhm,[†] Jörg Tatchen,[‡,§] Daniel Krügler,[†,#] Karl Kleinermanns,*[,†] Michael G. D. Nix,[||] Tracy A. LeGreve,[⊥] Timothy S. Zwier,*[,⊥] and Michael Schmitt*[,†]

Institut für Physikalische Chemie I, Heinrich-Heine-Universität, D-40225 Düsseldorf, Germany, Institut für Theoretische Chemie, Heinrich-Heine-Universität, D-40225 Düsseldorf, Germany, School of Chemistry, University of Bristol, Bristol BS8 1TS, U.K., and Department of Chemistry, Purdue University, 560 Oval Drive, West Lafayette, Indiana 47907-2084

Received: November 29, 2008

The vibronic spectrum of tryptamine has been studied in a molecular beam up to an energy of 930 cm^{-1} above the S_0-S_1 electronic origin. Rotationally resolved electronic spectra reveal a rotation of the transition dipole moment direction from ^1L_b to ^1L_a beginning about 400 cm^{-1} above the ^1L_b origin. In this region, vibronic bands which appear as single bands at low resolution contain rotational structure from more than one vibronic transition. The number of these transitions closely tracks the total vibrational state density in the ^1L_b electronic state as a function of internal energy. Dispersed fluorescence spectra show distinct spectroscopic signatures attributable to the ^1L_b and ^1L_a character of the mixed excited-state wave functions. The data set is used to extrapolate to a ^1L_a origin about 400 cm^{-1} above the ^1L_b origin. DFT-MRCI calculations locate a conical intersection between these two states at about 900 cm^{-1} above the L_a origin, whose structure is located along a tuning coordinate which is close to a linear interpolation between the two excited-state geometries. Along the branching coordinate, there is no barrier from ^1L_a to ^1L_b. A two-tier model for the vibronic coupling is proposed.

Introduction

A detailed picture of excited-state photophysics is often blurred by the fact that, even at low excess energies above the minimum of the lowest electronically excited state, crossings with *repulsive* electronic states happen, which frequently prevents spectroscopic investigations due to the loss of spectral resolution. We will show in the following that the photophysics of tryptamine in the first few hundred wavenumbers above the minimum of the lowest excite state is governed by a conical intersection (CI) between two *bound* states, which facilitates the spectroscopic observation of the implications of a low-lying CI involving two close-lying excited states.

Tryptamine (TRA) is a close analogue of tryptophan, one of only three aromatic amino acids that are responsible for much of the observed fluorescence of proteins. Tryptophan has served as a useful probe of its local environment in proteins because the emission wavelength and excited-state lifetime depend on its environment.[1−4] This sensitivity arises because of the close proximity of two $^1\pi\pi^*$ excited states, whose energy separation and relative energy ordering change with the polarity of the environment. Motivated by this fact, much experimental and theoretical effort has been directed at understanding the nature of these excited states and their interactions with one another.[3,5−9] Tryptamine has played a useful role as a somewhat simpler analogue of tryptophan, differing from it by removal of the carboxylic acid group.[10−17]

The ultraviolet chromophore of tryptamine and tryptophan is the indole ring. Indole and its substituted derivatives all have in common these two close-lying excited states, labeled as L_a and L_b (in the nomenclature of Platt,[18] modified to indole derivatives by Weber[19]), with transition dipole moments orthogonal to one another.[18] In addition, recent theoretical[20] and experimental[21,22] investigations have revealed the importance of a third, energetically close-lying, state of $^1\pi\sigma^*$ character, which plays a crucial role in its photodissociation.

The relative energetics of ^1L_a and ^1L_b in indole and its derivatives have been extensively probed. Dispersed fluorescence studies by Wallace[5] have assisted in the assignment of the vibronic structure of indole, including Herzberg−Teller bands. Further studies by Hager et al.[23] determined the effects of substitution on the indole chromophore. 3-Substitution causes a reduction in the ^1L_a energy, reducing the splitting between ^1L_a and ^1L_b (ΔE) and increasing the coupling between ^1L_a and ^1L_b near the ^1L_b origin. 3-Methylindole has its ^1L_a origin approximately 600 cm^{-1} above the ^1L_b origin.[23] Sammeth et al. were able to assign many of the vibronic bands in 3-methylindole to the ^1L_b and the ^1L_a state using polarized two photon fluorescence excitation spectra.[24] They locate the ^1L_a origin at 334 or 468 cm^{-1} above the ^1L_b origin. 1-Methylation also leads to a reduction in the state separation, although to a lesser extent. Due to the localization of the ^1L_b state on the benzene ring,[3,7] 5-substitution lowers the energy of this state and hence increases the excited-state splitting relative to the unsubstituted case.

High-level ab initio studies using the multiconfigurational second-order perturbation approach (CASPT2)[25] of indole have reproduced the vertical excitation energies with reasonable accuracy. The nature of the ^1L_a and ^1L_b potential surfaces has

* Corresponding authors, kleinermanns@uni-duesseldorf.de, Zwier@purdue.edu, and mschmitt@uni-duesseldorf.de.
[†] Institut für Physikalische Chemie I, Heinrich-Heine-Universität.
[‡] Institut für Theoretische Chemie, Heinrich-Heine-Universität.
[§] Present address: Chemical Physics Department, Weizmann Institute of Science, 76100 Rehovot, Israel.
[||] School of Chemistry, University of Bristol.
[⊥] Department of Chemistry, Purdue University.
[#] Present address: Bruker Daltonik GmbH, 28359 Bremen, Germany.

10.1021/jp810502v CCC: $40.75
Published on Web 02/20/2009

been studied less completely; Slater and Callis[26] used the configuration interaction singles (CIS) method to determine that the diabatic ^1L_b and ^1L_a states cross and identified an "avoided crossing" in the adiabatic surfaces as a result. Points of electronic near-degeneracy in polyatomic systems are often indicative of conical intersections,[27] lying nearby in the multidimensional configuration space.

Compared to indole, studies of tryptamine are complicated by the presence of the ethylamine side chain, which makes possible the presence of conformational isomers. Six different conformers were first identified by Park et al. on the basis of their saturation characteristics.[28] Philips and Levy used high-resolution ultraviolet spectroscopy to make first assignments for these conformers, identifying the presence of a seventh conformer unresolved in the first study.[13] The triply deuterated conformers were investigated by Wu and Levy.[29] Connell et al. performed a conformational analysis of tryptamine using rotational coherence spectra.[30] The two most stable conformers of tryptamine were investigated by Caminati using microwave spectroscopy.[31] Carney and Zwier[10] investigated all seven conformers using resonant ion dip infrared (RIDIR) spectroscopy in the region of the CH alkyl stretch vibrations and by UV−UV hole-burning spectroscopy, leading to a refinement of the conformational assignments. Dian et al. measured directly the energy thresholds between the different conformers of tryptamine using stimulated emission pumping hole filling and stimulated emission pumping induced population transfer spectroscopy.[32,33] The conformational equilibrium between different Anti conformers and the Gph(out) conformer was also studied experimentally and theoretically by Böhm et al.[34]

Two groups have recently returned to the high-resolution ultraviolet spectroscopy of TRA, confirming and refining earlier assignments for the conformers of TRA, and proving unequivocally that the $S_1 \leftarrow S_0$ transitions of all seven conformers are *a*-axis polarized, marking the S_1 state as the ^1L_b state.[11,12,15]

One consequence of the focus on the ground-state conformational preferences of tryptamine is that its vibronic transitions above the ^1L_b origin are not so well characterized due to the fact that the ultraviolet spectra of all seven conformers contribute to the spectrum. Recent DFT/MRCI calculations on the conformers of TRA with the BH-LYP functional place the L_b origin of the Gpy(out) conformer at 34841 cm^{-1} and the L_a origin at 35726 cm^{-1}, i.e., 885 cm^{-1} above the L_b origin.[16] The band type for the L_b state was correctly predicted as being predominantly *a*-type, while for the L_a state a nearly pure *b*-type transition was predicted.

Given this close proximity between L_b and L_a states, with energy separations of a few hundred cm^{-1}, and the anticipated possibility of a conical intersection not far above the minima of the two states, tryptamine offers an ideal system for searching for the presence of the L_a state and for determining the spectroscopic consequences of these two potential energy surfaces being in close proximity and near a conical intersection. The present study makes use of the UV hole-burning spectrum[10] to identify key vibronic transitions in the first 1000 cm^{-1} above the ^1L_b origin of the most stable conformation of TRA, assigned to the Gpy(out) conformation. High-resolution ultraviolet spectra of 10 of these bands have been recorded, identifying the number of bands present and their transition dipole moment direction. These are then combined with dispersed fluorescence spectra of these same transitions, leading to the identification of key spectral signatures in the emission ascribable to the mixed electronic character of the excited-state wave functions responsible for the emission. Evidence of ^1L_b/^1L_a coupling due to conical intersection induced mixing is presented and discussed in terms of a general model which is also consistent with the known spectroscopy of the indole chromophore itself.

Methods

Theoretical Methods. Structure optimizations were performed employing the valence triple-ζ basis set with polarization functions (d,p) from the Turbomole library.[35,36] The equilibrium geometries of the electronic ground and the lowest excited singlet states were optimized for a restricted closed shell KS determinant using the B3-LYP density functional.[37,38] Furthermore, we optimized the geometries of the low-lying L_a and L_b electronic singlet states by means of a TDDFT gradient.[39] All DFT or TDDFT calculations were carried out utilizing the Turbomole package, version 5.6.[40] Ground-state vibrational frequencies have been calculated through analytical second derivatives using the aoforce module[41,42] implemented in Turbomole Version 5.8. Excited-state vibrational frequencies were calculated using numerical differentiation of analytic gradients using the NumForce script from Turbomole Version 5.8.

The conical intersection (CI) of the L_a and L_b states has been optimized at the CASSCF (10,9) level of theory with the 6-311G(d,p) basis set using the Gaussian03 program package[43] with the direct algorithm for location of the lowest energy point on a potential surface crossing as described by Bearpark et al.[44] This procedure results in the gradient difference vector and the interstate coupling vector which together form the two-dimensional branching space from which the $(n - 2)$-dimensional intersection space is constructed.[45]

The singlet-state energies, wave functions, and transition dipole moments were calculated using the combined density functional theory/multireference configuration interaction (DFT/MRCI) method by Grimme and Waletzke.[46] The configuration state functions (CSFs) in the MRCI expansion are constructed from Kohn−Sham (KS) orbitals, optimized for the dominant closed shell determinant of the electronic ground-state employing the BH-LYP[38,47] functional. All valence electrons were correlated in the MRCI runs, and the eigenvalues and eigenvectors of the two lowest singlet states were determined. The initial set of reference configuration state functions was generated automatically in a complete active space type procedure (including all single and double excitations from the five highest occupied molecular orbitals in the KS determinant to the five lowest virtual orbitals) and was then iteratively improved. The MRCI expansion was kept moderate by extensive configuration selection. The selection of the most important CSFs is based on an energy gap criterion as described by Grimme and Waletzke.[46] Only those configurations were taken into account whose energy did not exceed a certain cutoff energy. The energy of a given configuration was estimated from orbital energies within the selection procedure. The cutoff energy was given by the energy of the highest desired root as calculated for the reference space plus a cutoff parameter $\delta E_{sel} = 1.0 E_H$. The latter choice has been shown to yield nearly converged results in ref 46. The so obtained MRCI space was spanned by about 200000 singlet CSFs from approximately 50 reference configurations.

Experimental Methods

Rotationally Resolved Electronic Spectroscopy. High-resolution spectra were taken by the Schmitt group at Heinrich-Heine-Universität in Düsseldorf. The experimental setup for the rotationally resolved laser induced fluorescence is described in detail elsewhere.[48] Briefly, it consists of a ring dye laser

(Coherent 899-21) operated with Kiton Red, pumped with 7 W of the frequency doubled output of a diode pumped Yb:YAG disk laser (ELS). About 600−700 mW of the fundamental dye laser output is coupled into an external folded ring cavity (Spectra Physics) for second harmonic generation.

The molecular beam is formed by expanding tryptamine heated to 160 °C and seeded in 300−700 mbar of argon through a 100 μm hole into the vacuum. The molecular beam machine consists of three differentially pumped vacuum chambers that are connected by two skimmers (1 and 3 mm, respectively) in order to reduce the Doppler width to 25 MHz. The molecular beam is crossed at right angles in the third chamber with the laser beam ≈360 mm downstream of the nozzle. The emitted fluorescence is collected perpendicularly to the plane defined by laser and molecular beam by imaging optics. The total fluorescence is detected on the photocathode of an UV enhanced photomultiplier tube whose output is recorded by a PC-based photon counter card. The relative frequency is determined with a home-built quasi-confocal Fabry−Perot interferometer. The absolute frequency is determined by recording the iodine absorption spectrum and comparison of the transitions to the tabulated lines of the iodine atlas.[49]

Dispersed Fluorescence Spectroscopy. Dispersed fluorescence (DF) spectra were recorded at Purdue University. The experimental setup is described in detail elsewhere.[50] Briefly, the collimated, frequency doubled output of a Nd:YAG (Innolas)-pumped dye laser (Radiant Dyes Narrowscan) operated at 20 Hz was used as the ultraviolet source. The supersonic expansion is formed by heating tryptamine to 125 °C and entraining it in helium carrier gas at 500−1500 mbar using a high-temperature pulsed valve (General Valve, Series 9, 0.8 mm diameter) operating at 20 Hz. The total fluorescence is dispersed by a Jobin Yvon 750i monochromator equipped with a 2400 line/mm grating, using slit widths of 50 or 100 μm, with a resolution of 4 or 8 cm^{-1} fwhm. The dispersed fluorescence signal is detected by a thermoelectrically cooled (−75 °C) CCD camera (Andor Technology). Scattered light and background are removed from the spectra by taking a background scan with the time delay between the pulsed valve opening and laser pulse shifted out of the gas pulse. The reported spectra are then the difference between DF scans taken with and without the fluorescence present.

Experimental Results

Figure 1a shows the conformer-specific UV hole-burning vibronic spectrum of the Gpy(out) conformer of TRA, hereafter TRA(A), from Carney et al.[10] over a range that extends from the S_1 origin at 34915.64 cm^{-1} to about 800 cm^{-1} above it. This spectrum is reproduced here to show that the discussed bands in the LIF spectrum are free from influences from other conformers. Figure 1b shows the LIF excitation spectrum in the same range, labeled with the wavenumber positions of the bands for reference in what follows. This spectrum was taken under laser power conditions that minimize saturation effects. DF spectra have been taken of all bands labeled in the UV hole-burning spectrum. Very weak bands at 123 and 332 cm^{-1} are not seen at the scale shown in Figure 1b under unsaturated conditions. All vibronic bands except the one at 229 cm^{-1} above the origin were investigated by rotationally resolved electronic spectroscopy.

Rotationally Resolved Spectra of the Vibronic Bands of Tryptamine. The high-resolution ultraviolet spectrum of the $S_1 \leftarrow S_0$ origin of TRA(A) has been reported earlier.[11,15] The results of the analysis of this band are contained in Table 1.

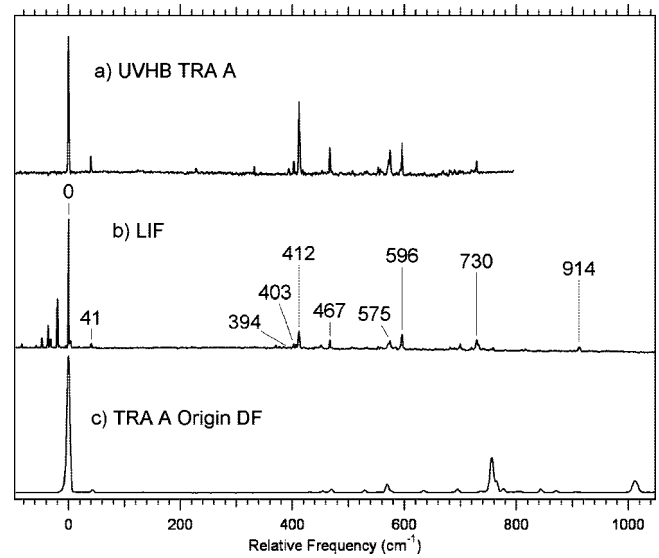

Figure 1. (a) UV−UV hole-burning spectrum of TRA(A). (b) Laser induced fluorescence spectrum of TRA(A). (c) Dispersed fluorescence from the ^1L_b origin of TRA(A), showing the breakdown of mirror symmetry in the 400−600 cm^{-1} region.

The rotational structures of all vibronic bands are fit to a rigid rotor Hamiltonian using an automated genetic algorithm approach described in detail in refs 51−53. The fit yields the changes of the rotational constants upon electronic excitation, the center frequencies ν_0 of the vibronic bands, and the orientation of the transition dipole moments with respect to the inertial axes (Table 1). The data reported in Table 1 show that the $S_1 \leftarrow S_0$ origin is mainly polarized along the inertial *a*-axis (85%, cf. Table 1), identifying it as arising from the ^1L_b state. The bands at 41, 123, and 332 cm^{-1} all follow predominant *a*-type selection rules as can be seen from Table 1 and from the spectra in the Supporting Information. For the vibronic band at 0,0 + 403 cm^{-1} a sudden change in the appearance of the spectrum can be observed. The central *Q*-branch vanishes and the spectrum can be fit by using nearly exclusively *b*-type selection rules, indicating a rotation of the transition dipole moment orientation by 90°. Spectra a and c of Figure 2 contrast the very different rotational structure of the bands at 332 and 403 cm^{-1}. Tryptamine offers a very favorable situation for the observation of this effect: since the transition dipole moment of the origin band is oriented nearly parallel to one of the main axes of inertia (in this case the *a*-axis), there is no ambiguity as to the sign of the TDM angle, which cannot be determined from the observation of relative intensities of rovibronic spectra. The situation in other chromophores of this type is complicated by the fact that the TDM makes an angle with the inertial axes. In indole for example the angle θ of the TDM with the *a*-axis is determined to ±38°.[54] Since the L_a and L_b orientations differ by approximately 90°, a value of the TDM angle close to 45° makes the analysis of the higher vibronic bands of indole very difficult.

The high-resolution spectrum of the strong transition 412 cm^{-1} above the S_1 origin is shown in Figure 2e. It is composed of two components, separated by 21425 MHz, with similar rotational constants in the electronically excited states. As with the 403 cm^{-1} band, both components are fit as nearly pure *b*-type bands (cf. Table 1), indicating that also for this vibronic band the transition dipole moment is rotated by 90° from its direction at the S_1 origin.

The following bands at 575 and 596 cm^{-1} (shown in the Supporting Information), are composed of three and four

TABLE 1: Molecular Parameters for the Vibronic Bands of the TRA(A)[a]

band	ν_0	$\Delta\nu_0$	ΔA	ΔB	ΔC	μ_a^2	μ_b^2	μ_c^2	I_{rel}
A	34915.64		−7.00	−9.36	−6.98	0.85	0.05	0.10	
A + 41	34956.77		−0.14	−10.79	−8.10	0.99	0.00	0.01	
A + 123	35038.41		−5.94	−10.14	−7.53	0.93	0.03	0.05	
A + 332	35248.22		−7.66	−9.13	−6.37	0.97	0.00	0.03	
A + 403	35318.02		−4.86	−10.04	−7.36	0.12	0.85	0.03	
A + 412	35327.12	0.0	−2.91	−10.36	−7.69	0.11	0.85	0.04	1.00
A + 412		21425.21	−4.81	−10.15	−7.49	0.10	0.81	0.09	0.76
A + 467	35382.52	0.0	0.81	−10.93	−8.61	0.00	0.99	0.01	1.00
A + 467		3233.15	2.50	−11.42	−8.27	0.00	0.99	0.01	0.95
A + 575	35490.36	0.0	−4.26	−10.30	−7.54	0.09	0.80	0.11	0.91
A + 575		21502.24	3.63	−11.55	−8.80	0.05	0.83	0.12	0.50
A + 575		40379.34	−0.59	−11.12	−7.76	0.30	0.70	0.17	1.00
A + 597	35511.74	0.0	−2.16	−9.26	−6.29	0.14	0.85	0.01	1.00
A + 597		2921.93	−0.24	−9.93	−8.46	0.09	0.90	0.01	0.85
A + 597		4042.67	−2.08	−11.24	−6.73	0.24	0.74	0.02	0.38
A + 597		5059.51	3.60	−11.66	−7.86	0.15	0.85	0.00	0.48
A + 730	35645.28	0.0	2.51	−10.74	−6.99	0.44	0.46	0.10	0.56
A + 730		7559.46	2.07	−11.33	−8.29	0.72	0.27	0.01	1.00
A + 730		12584.75	5.85	−11.92	−5.96	0.30	0.66	0.04	0.68
A + 730		18433.23	3.62	−9.26	−5.19	0.36	0.63	0.01	0.31
A + 913		14 Q-branches							

[a] All values are given in megahertz except for the origin frequencies ν_0, which are given in cm^{-1}. $\Delta\nu_0$ gives to the difference of band origins for very nearby or partially overlapping bands as frequency difference in megahertz to the band given in the preceding row(s). The dimensionless squared transition moment components have been calculated using the relations $\mu_a^2 = (\mu \sin\phi \cos\theta)^2$, $\mu_b^2 = (\mu \sin\phi \sin\theta)^2$, and $\mu_c^2 = (\mu \cos\phi)^2$ from the fitted parameters θ and ϕ. Relative intensities refer to the strongest component of the vibronic sub-bands. Ground-state rotational constants for TRA(A) are fixed to the microwave values from ref 31.

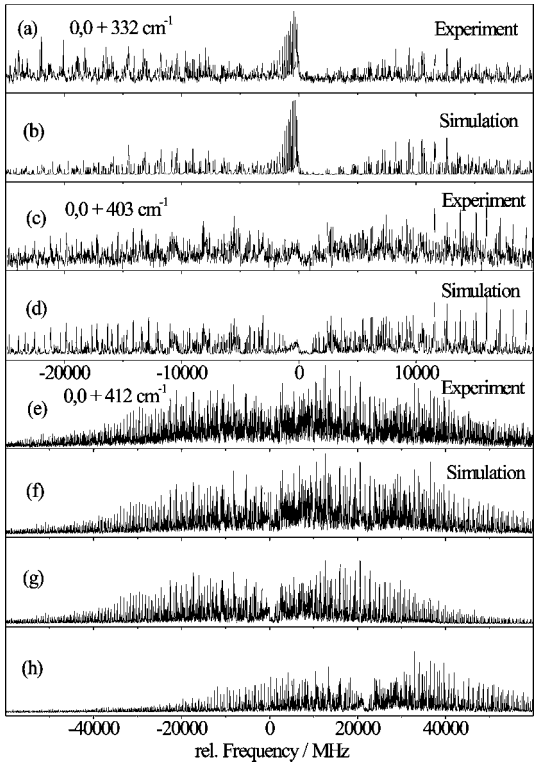

Figure 2. (a) Rotationally resolved spectrum of the 0,0 + 332 cm^{-1} band. (b) Simulation of the 0,0 + 332 cm^{-1} band using the molecular constants from Table 1. (c) Rotationally resolved spectrum of the 0,0 + 403 cm^{-1} band. (d) Simulation of the 0,0 + 403 cm^{-1} band using the molecular constants from Table 1. (e) Rotationally resolved spectrum of the 0,0 + 412 cm^{-1} band. (f) Simulation using the molecular constants from Table 1. (g) and (h) Deconvolution into the two sub-bands comprising the 412 cm^{-1} vibronic band.

components, respectively each of which again is a nearly pure *b*-type band. The vibronic band at 730 cm^{-1} (shown in the Supporting Information) shows a strong central *Q*-branch, but there are three other *Q*-branches barely visible in the spectrum. Using the genetic algorithm technique, this spectrum has been fit as the sum of four components (the bottom four traces of the figure), all of which have an *ab*-hybrid band structure with the TDM direction varying from one sub-band to the next (Table 1). The last investigated band at 930 cm^{-1} (shown in the Supporting Information) is too congested to be analyzed even using the evolutionary strategy. Nevertheless, the inspection of the band shape shows that the band is composed of at least 14 components with intense *Q*-branches.

Dispersed Fluorescence Spectra through Vibronic Bands of Tryptamine. Figure 1c shows a closeup of the first 800 cm^{-1} of the dispersed fluorescence spectrum obtained via excitation of the ^1L_b electronic origin. The spectrum is dominated by resonance fluorescence, indicating that the geometry change between S_0 and L_b states is relatively small. The most intense band in the DF spectrum appears at 765 cm^{-1}, ascribable to a ring-breathing mode fundamental,[17] as has been discussed previously.

The comparison between the LIF spectrum (trace b of Figure 1) and the S_1 origin DF spectrum of TRA(A) (trace c of Figure 1) shows a striking lack of symmetry, especially in the strong transitions in the LIF spectrum in the 400−600 cm^{-1} region, which are absent in the DF spectrum. This asymmetry suggests the possibility that transitions in this region gain their intensity from a second excited state.

DF spectra are shown in Figure 3 for the most important vibronic bands in the TRA(A) holeburning spectrum, with all other DF spectra of other bands of TRA(A) shown in the Supporting Information. The emission spectra obtained by pumping the vibronic bands at +394 and +403 cm^{-1} relative to the origin are shown in spectra a and b of Figure 3. The strongest band in emission from the +394 cm^{-1} appears at an S_0 energy of 453 cm^{-1}, with some weaker cross-sequence bands at 365 and 417 cm^{-1}. The strongest band in the +403 cm^{-1} emission spectrum appears at 554 cm^{-1}, with weaker cross-sequence bands at 381 and 453 cm^{-1}. In each case, these strong transitions serve as false origins for vibronic bands built off of

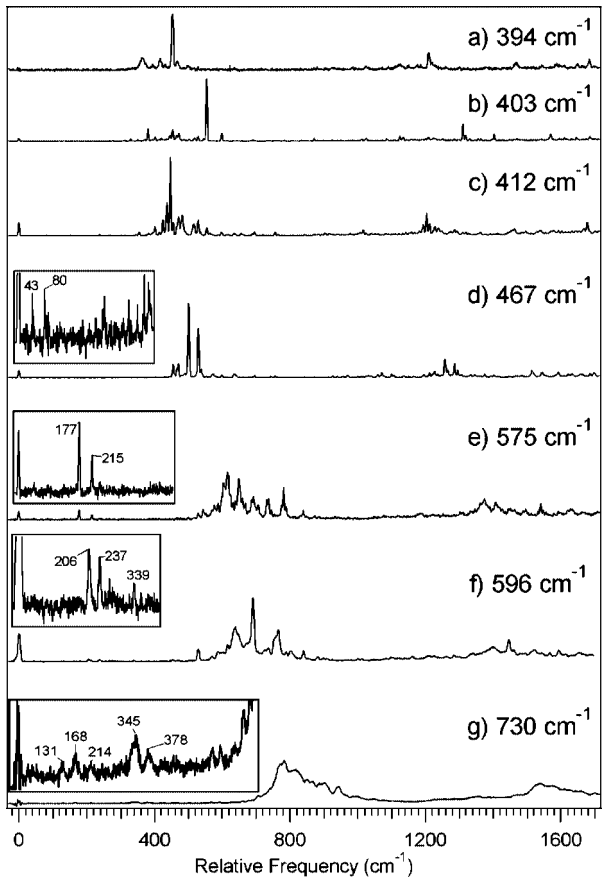

Figure 3. DF spectra recorded at various vibronic levels with the following position relative to ^1L_b origin in cm^{-1}: (a) +394, (b) +403, (c) +412, (d) +467, (e) +575, (f) +596, (g) +730. The insets show the low-frequency region in magnification, revealing weak fluorescence to low frequency modes.

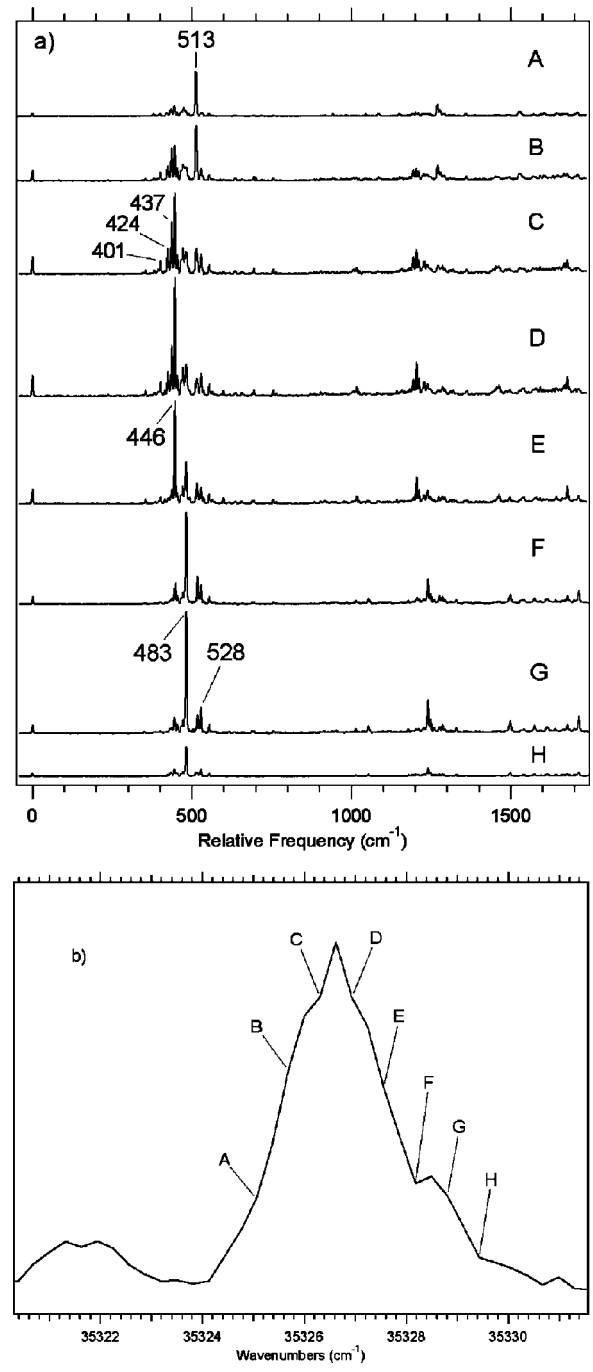

Figure 4. (a) DF spectra recorded at various positions within the band contour of the +412 cm^{-1} band. (b) The band contour, showing the excitation wavelengths used to record spectra in (a).

them. Since the S_1 origin emission (Figure 1c) exhibits a strong $\Delta v = 0$ Franck−Condon propensity, application of this same propensity to the vibrational level at 394 cm^{-1} in the excited state leads to an assignment of the transition at 454 cm^{-1} to a ground-state level with the same quantum numbers. Similarly, the 403 cm^{-1} excited-state level corresponds to a 554 cm^{-1} level in the ground state.

Emission from the peak of the vibronic band at +412 cm^{-1}, the most intense vibronic band in the excitation spectrum, is shown in Figure 3c. Figure 4a presents a series of eight DF spectra taken while stepping the excitation wavelength across the entire band at 412 cm^{-1} in order to resolve the emission from various components of the band. The excitation wavelengths are displayed on the band contour in Figure 4b. The strong emission bands, particularly in the 400−500 cm^{-1} region, vary in intensity significantly across the band, with certain transitions rising in intensity and then decaying away over the space of two or three spectra. The two strongest emission bands are observed at 446 and 483 cm^{-1}, with the former maximizing its intensity at position D, while the latter transition goes through its intensity maximum at position G. Cross sequence bands are prominent and form a dense clump of lines around the diagonal transition.

Figure 4 clearly shows that the +412 cm^{-1} band is composed of at least two, and as many as four, different vibronic bands. Interestingly, resonance fluorescence (to the S_0 zero point level) is observed in association with certain specific subcomponents within the band, a point to which we will return in the Discussion. Scattered light has been removed from these spectra by means of background subtraction.

Figure 3d shows the DF spectrum recorded at the peak of the 467 cm^{-1} vibronic band. The strongest emission band in the spectra appears at 500 cm^{-1}, with a second strong band at 529 cm^{-1}. No distinction between these peaks could be made by stepping over the band profile (not shown).

Figure 3e presents the DF spectrum at the peak of the 575 cm^{-1} band. The vast majority of the emission occurs in the 500−800 cm^{-1} region, which serves as false origin for ring-mode transitions built off of the bands in this region. DF spectra recorded by exciting at several positions across the band profile of the 575 cm^{-1} band vary across the absorption profile (shown in the Supporting Information). There is significant off-diagonal

fluorescence, making assignment of individual diagonal transitions difficult due to the large number of transitions involved. Low-frequency emission bands appear at 177 and 215 cm^{-1}, which are shown in the inset in Figure 3e. These spectra also display resonance fluorescence, a feature held in common with the emission from the 412 and 467 cm^{-1} bands.

Finally, the emission spectra obtained by pumping the 596 and 730 cm^{-1} vibronic bands are shown in spectra f and g of Figure 3, respectively. A multitude of cross-sequence bands broaden the main fluorescence feature, while a number of weak, low-frequency transitions are observed (insets with spectra f and g of Figure 3).

The low-frequency bands appearing in the DF spectra from levels 570−730 cm^{-1} above the S_1 origin (Figure 3, spectra d−g), are highly unusual. The observation of such a structure suggests the mixing of a second vibronic wave function into these levels, one with much less vibrational energy than the S_1 excess photon energy.

Theoretical Results

Vibrational Frequencies and Herzberg−Teller Coupling. Table S1 in the Supporting Information shows the frequencies of all vibrational modes of the Gpy(out) conformer of tryptamine in the ground and electronic excited state, obtained from density functional calculations and time-dependent DFT with the B3-LYP functional using the TZVP basis set. The descriptions of the modes follow the suggestion of Varsanyi[55] for ortho-dilight-substituted benzene derivatives and are complemented for vibrations of the pyrrole ring following the scheme given in ref 56 and for the vibrations of the ethylamino group. In an unsymmetrical molecule of this size the unequivocal description of modes poses a problem. Therefore the most authoritative description of the modes is given by a graphical visualization program. Molden frequency files (.molf) containing geometries and vibrational modes investigated in this study can be obtained from the authors homepage at http://www-public.rz.uni-duesseldorf.de/~mschmitt/Gaussian_logs.html.

The transition dipole moment for a transition between an initial electronic state $|m,v\rangle$ and a final electronic state $|n,w\rangle$ is defined as

$$M_{vw} = \langle v|\mu_{mn}(Q)|w\rangle \tag{1}$$

with the electronic transition dipole moment $\mu_{mn}(Q)$

$$\mu_{mn}(Q) = \langle \Psi_m|\mu|\Psi_n\rangle; \qquad \mu = \sum_g e r_g \tag{2}$$

where r_g is the position vector of the gth electron. The dependence of the electronic transition dipole moment μ_{mn} from the nuclear coordinates can be approximated by expanding μ_{mn} in a Taylor series about the equilibrium position at Q_0. Truncation of the expansion after the second expansion term and inserting into eq 1 yields the transition dipole moment in the Franck−Condon−Herzberg−Teller (FCHT) approximation

$$M_{mn} = \mu_{mn}(Q_0)\langle v|w\rangle + \sum_i \left(\frac{\partial \mu_{mn}}{\partial Q_i}\right)_{Q_0} \langle v|Q_i|w\rangle \tag{3}$$

The evaluation of the Franck−Condon (FC) integrals $\langle v|w\rangle$ in eq 3 is straightforward using the recursive relations of Doktorov,[57] which uses the Duschinsky transformation[58] to reduce the integrals over the vibrations in the electronic ground and excited state to integrals over the ground-state vibrational wave functions only. For the evaluation of the Herzberg−Teller (HT) terms

$$\sum_i \left(\frac{\partial \mu_{mn}}{\partial Q_i}\right)_{Q_0} \langle v|Q_i|w\rangle$$

in eq 3 the partial derivatives of the transition dipole moment with respect to the normal modes must be calculated. These derivatives of μ_{mn} were determined numerically from DFT/MRCI calculations of the respective state using symmetric finite differences

$$\left(\frac{\partial \mu_{mn}}{\partial Q_i}\right)_{Q_0} = \frac{\mu_{mn}(Q_0 + \Delta Q_i) - \mu_{mn}(Q_0 - \Delta Q_i)}{2\Delta Q_i} \tag{4}$$

They are given along with the respective normal modes and their approximative description in Table S1 of the Supporting Information.

The integrals $\langle v|Q_i|w\rangle$ from the HT terms in eq 3 can be calculated from the FC integrals using the relation

$$\langle v|Q_i|w\rangle = \sqrt{\frac{\hbar}{2\omega_i}}[\sqrt{w_i}\langle v|w_1,\ldots,\ (w_i-1),\ldots,\ w_N\rangle + \sqrt{w_i+1}\langle v|w_1,\ldots,\ (w_i+1),\ldots,\ w_N\rangle] \tag{5}$$

Figure 5 presents a comparison of the pure FC structure predicted by the DFT and TDDFT calculations for the $^1L_b \leftarrow S_0$ (Figure 5a) and $^1L_a \leftarrow S_0$ (Figure 5b) transitions using the Hessian obtained at the same level of theory and the vibronic FCHT structure obtained as described above. Note that, despite the presence of vibronic terms, the excitation spectrum for both transitions is dominated by vertical emission to the electronic origin. Nevertheless, the intensity of the transition predicted at 458 cm^{-1} is considerably increased by HT coupling, and other vibrations in this region also gain some intensity. These

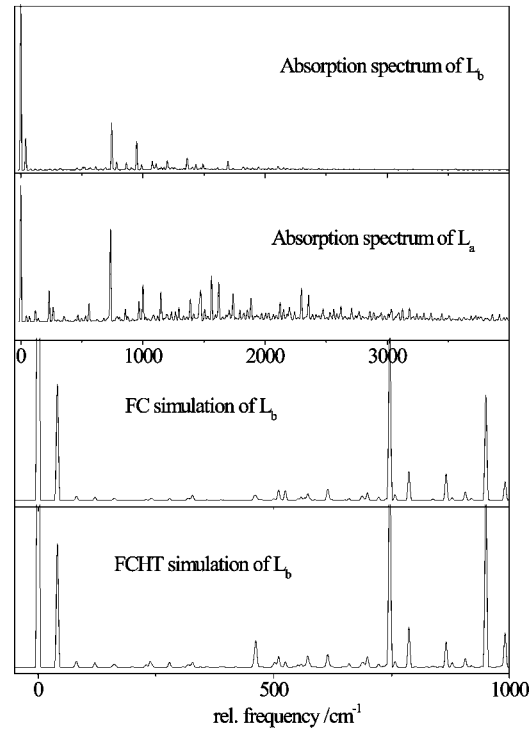

Figure 5. Franck−Condon simulation of the L_b (trace a) and L_a (trace b) absorption spectra of tryptamine using the Hessian for the electronic ground state from B3-LYP/TZVP calculations and for the L_a and L_b states from time-dependent B3-LYP/TZVP calculations. The two lowest traces compare the simulations of the first 1000 cm^{-1} of the absorption spectrum of the L_b state using only the FC terms from eq 3 (trace c) and including the Herzberg−Teller terms (trace d).

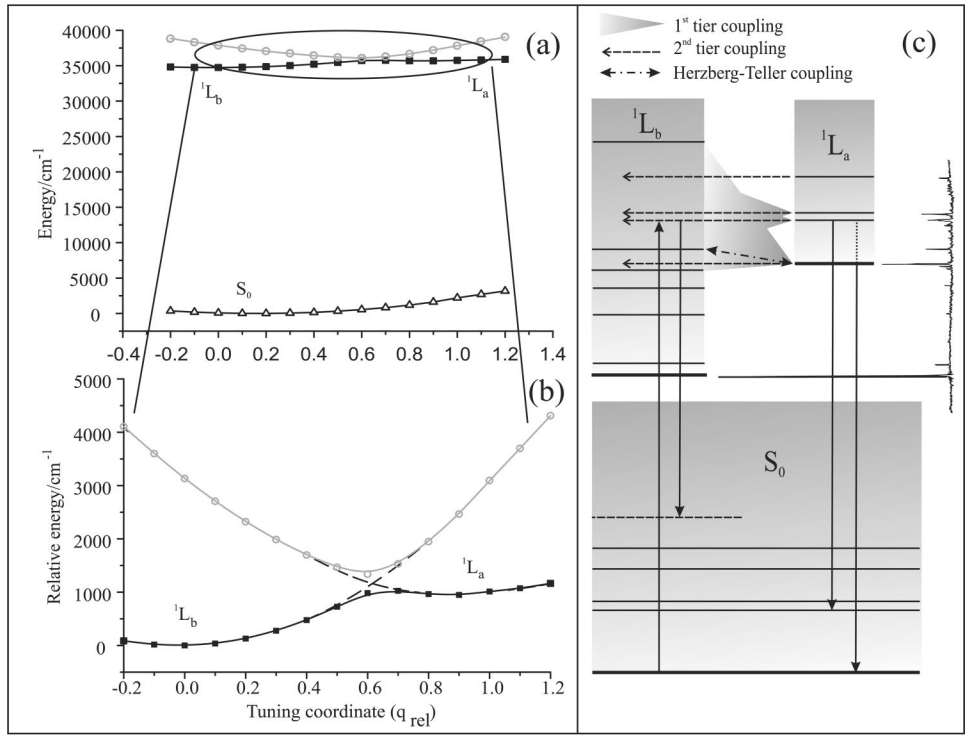

Figure 6. (a) 1D cut through the adiabatic multidimensional potential energy surfaces (PES) of S_0 (unfilled triangles), S_1 (filled squares), and S_2 (open circles) computed at the DFT-MRCI level of theory, along a coordinate connecting the L_b and L_a minima, along which the conical intersection of these two surfaces lies. Energies are relative to the S_0 minimum. (b) Expansion of the energy scale in (a) to show the S_1/S_2 conical intersection, with energies relative to the L_b minimum of the S_1 surface. (c) Schematic model of vibronic mixing in the L_b/L_a system. Dominant vibration fundamental levels of both states are indicated by solid lines. Mixing occurs via three mechanisms in the region above 400 cm^{-1} and levels have mixed L_b/L_a character. Strong "first-tier" mixing stretches over tens of cm^{-1} and much weaker "second-tier" mixing connects background L_a fundamentals with L_b background combination levels within 1 cm^{-1} of them. Herzberg−Teller interactions further complicate the model (most strongly at +467 cm^{-1}). See the text for further details.

calculations can serve as a starting point for evaluation of vibronic coupling between ^1L_b and ^1L_a. However, the close energetic proximity of these two states could lead to a breakdown of the $\Delta v = \pm 1$ vibronic coupling selection rule that arises from this analysis. Thus, pure vibronic coupling within the limits of the validity of the Born−Oppenheimer approximation cannot be responsible alone for the observed intensity effects around 400 cm^{-1}. In the following section we will show, that a close-by conical intersection between the two excited states is the likely cause of the large intensity gain of vibronic bands in this spectral region.

The identification of excited-state vibrations is complicated by the substantial mixing of modes relative to the ground state. To investigate this effect we calculated the Duschinsky matrix,[58] which shows the mixing of the normal coordinates of the two states. A portion of this matrix is shown in Table S2 of the Supporting Information. In the low-frequency range, the torsional modes of the ethylamino side chain in the excited state are directly related to only one ground-state vibration. However, strong mixing is found for modes around 400 cm^{-1}.

The Conical Intersection between ^1L_b and ^1L_a. CASSCF searches have been carried out in order to locate a conical intersection between the ^1L_b and ^1L_a states. These calculations yielded a structure which lies extremely close to a linear coordinate linking the ^1L_b and ^1L_b minima, with an energy only slightly above the ^1L_a origin. Unfortunately, these calculations do not account for dynamic electron correlation and produce an artificially high value for the $^1L_b/^1L_a$ state separation. Knowing from the CASSSCF calculations that the conical intersection is located very close to a linearly interpolated path between the two excited-state minima, we calculated an improved energy profile along this path using the DFT/MRCI method. DFT/MRCI has been proven before to yield very reliable absolute values of vertical and adiabatic excitation energies in general[46] and for tryptamine especially.[16] The result is shown in Figure 6. The predicted CI is located less than 1000 cm^{-1} above the ^1L_b minimum. Since our DFT/MRCI path only resembles a linearly interpolated path (no analytical gradients are available for DFT/MRCI), this value is an upper limit for the energy difference. Thus, the calculations predict a CI close to the region where the experimental intensity perturbations are found. Furthermore, the DFT/MRCI calculations predict a very shallow L_a minimum along this coordinate, so that zero-point motion alone is sufficient to completely couple ^1L_a and ^1L_b levels in the region of the ^1L_a origin.

Taking the branching coordinate of the CI into account, the CASSCF calculations predict the existence of a minimum energy pathway (MEP) from ^1L_a to ^1L_b minima that is barrierless. Given this prediction, one might plausibly expect not to find a single, pure ^1L_a origin or other ^1L_a vibronic bands in the spectrum but instead that the oscillator strength from each ^1L_a transition could be spread over several bands in the region due to strong mixing between the two states. We would also anticipate a breakdown of the $\Delta v = \pm 1$ Herzberg−Teller selection rules in coupling the two states.

Discussion

The experimental and calculated results just described serve as the basis for refinement of earlier models postulated to describe the spectroscopy and photophysics of trypt-

amine,[1,6,7,16,20,59,60] and particularly the interactions between ^1L_b and ^1L_a states that appear within a few hundred cm^{-1} of the ^1L_b origin.

The Evidence for $^1L_a/^1L_b$ Mixing and Location of the ^1L_a Origin. Here we summarize the key experimental observations for which any model of $^1L_a/^1L_b$ mixing in TRA must account. The origin and low-lying vibronic bands up to 394 cm^{-1} above the S_1 origin are unmixed ^1L_b levels. In particular, the S_0-S_1 origin transition (34915.64 cm^{-1}) exhibits a nearly pure *a*-type spectrum with a strong central *Q*-branch, showing the transition dipole moment is oriented along the inertial *a*-axis. This orientation belongs to the L_b state in Platt's nomenclature.[18,19] By contrast, a *b*-type contour, which lacks the central *Q*-branch, is the anticipated signature of the L_a state. The origin band dispersed fluorescence (Figure 1b) is simply interpreted in terms of dominant resonance fluorescence ($\Delta v = 0$) and further bands due to strong Franck−Condon factors to vibrational levels of S_0 at 756 and 1229 cm^{-1}, which reflect the geometry changes in the indole ring associated with the ^1L_b state.

The first vibronic bands of S_1 also show ^1L_b type transition dipole moments (see Table 1), indicating that there is no significant mixing of ^1L_a character into these levels. Dispersed emission spectra recorded at the +41, +229, +332, and +394 cm^{-1} vibronic transitions all show vertical emission to a false origin, corresponding to $\Delta v = 0$ transitions as expected for unperturbed ^1L_b vibronic levels. The emission is governed by diagonal transitions, weak cross sequences, and an absence of low frequency emission bands.

There is a lack of reflection symmetry between the S_1 origin DF spectrum (Figure 1c) and the LIF spectrum (Figure 1b), suggesting immediately that the strong bands at +403, +412, +467, +575, and +596 cm^{-1} in excitation gain their oscillator strength from non-Franck−Condon induced processes. In particular, the +412 cm^{-1} band has an excitation oscillator strength one-fifth that of the ^1L_b origin, whereas in emission its relative intensity is <1%.

One possible interpretation is that these bands between 403 and 596 cm^{-1} are ^1L_b bands, which gain their intensity from Herzberg−Teller coupling to the nearly isoenergetic ^1L_a state. The derivatives of the transition dipole moment with respect to the normal modes, given in Table S1 of the Supporting Information are large in the range between mode 9b, calculated at 458 cm^{-1} in the S_1 state and mode 17a calculated at 698 cm^{-1}, indicating HT coupling to be important in this frequency range. In this picture, e.g., the 467 cm^{-1} band gains its intensity from Herzberg−Teller coupling (or its vestiges) between the two states via an in-plane fundamental of 467 cm^{-1} in ^1L_b, analogous to the 480 cm^{-1} HT band in indole.[61] Comparison of calculated modes for indole and TRA(A) suggests that the (ν_{6b}) HT mode should occur at ~530 cm^{-1} in S_0 TRA(A), shifted 10 cm^{-1} down from its value in indole. Assuming a similar shift in S_1, one can reconcile the observation of this band at +467 cm^{-1} (cf. +480 in indole). The second subcomponent of the +467 band is probably a ^1L_b background level of complex vibronic character which is nearly isoenergetic with the HT-induced band and gains oscillator strength from it. It is likely anharmonically mixed with the first in the beginnings of IVR. Further assignments in this region are difficult due to the strongly mixed character of the S_1 modes (cf. the Duschinsky matrix in Table S2 of the Supporting Information). Nevertheless, the intensity gain through conventional HT coupling is much smaller than what is observed in the experiment. Figure 5 implies an increase of the intensity of the calculated bands at 458 and 462 cm^{-1} by a factor of 5 through HT coupling, while the experimentally observed bands at 412 and 467 cm^{-1} are the strongest bands in the absorption spectrum, requiring a gain factor through HT coupling of almost 20.

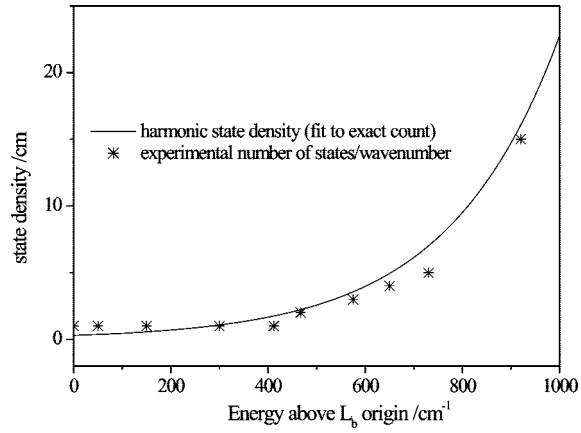

Figure 7. Harmonic state density as a function of the internal energy above the ^1L_b origin of TRA(A), calculated using exact count of the harmonic levels. Asterisks denote the observed number of sub-bands in the rotationally resolved spectra.

Consistent with these facts, all transitions between 403 and 596 cm^{-1} are nearly pure *b*-type bands (Table 1) and therefore derive their oscillator strength in excitation from the ^1L_a rather than the ^1L_b excited state. Beginning with the 412 cm^{-1} transition, all bands in the UV hole-burning spectrum are actually composed of two or more rotationally resolved vibronic transitions, with band origins separated by less than 1 cm^{-1} (cf. Table 1). This was shown unequivocally by the high-resolution scans, which stimulated interest in tuning through the band profiles to record DF spectra at several different excitation wavelengths. These spectra showed significant changes with position in the band profile, consistent with the sub-bands each carrying unique spectral signatures in emission.

The bands at +730 and +913 cm^{-1} are composed of 4 and 14 sub-bands, respectively all of which show clear *Q*-branches that reflect their mixed *a*/*b* hybrid band character (Table 1). In the +730 cm^{-1} transition, the TDM direction varies from one sub-band to the next. The +730 and +913 cm^{-1} transitions are both ascribable (nominally) to strong ^1L_b vibronic transitions common to indole and its derivatives, associated with in-plane indole ring fundamentals.[62] The strong admixture of *b*-type band character (which varies from one sub-band to the next) indicates that these ^1L_b vibronic levels are also mixed strongly with ^1L_a.

The DF spectra of Figure 3 all show dominant emission to ground state levels with positions consistent with their excitation energy above the ^1L_b origin. This emission reflects the ^1L_b character of the excited-state level(s), which is dominated by vertical emission back to ground-state levels with the same quantum number makeup as the excited-state levels. This emission varies from one sub-band to the next, consistent with these individual transitions having different makeup of their ^1L_b vibronic character.

It is important to note that the number of transitions contributing to the band profiles above 412 cm^{-1} closely tracks the calculated vibrational density of states of the ^1L_b state of TRA(A). Figure 7 compares the ^1L_b harmonic vibrational state density with the number of sub-bands per cm^{-1} observed by the high-resolution scans. The close match of the experimental observation with the exact count state density strongly suggests that the observed sub-bands arise from near-degenerate ^1L_b vibronic levels and that the vibronic coupling to these levels

that provides their oscillator strength is indiscriminate in that essentially the full density of states is observed.

Thus, within this model, the experimentally observed bands are all described as vibronic bands of the ^1L_b state, which gain their oscillator strength (and band type) by nonadiabatic coupling to the ^1L_a state, which has its origin at (or close to) $0,0(^1L_b) + 412$ cm^{-1}. The coupling is stronger than what is expected from HT theory, pointing to another coupling mechanism, which will be discussed in the following section. No ^1L_a bands are observed directly, neither in absorption nor in emission in this model.

All the transitions between 403 and 730 cm^{-1} have a small component of the emission that begins at the S_0 zero-point level (403, 412, 467 cm^{-1} transitions) and then shifts to low-lying S_0 levels above the zero-point by an amount roughly equal to their excited-state excess energy above 412 cm^{-1}. This low-frequency emission is highlighted in the insets of spectra d−g of Figure 3. These transitions end in energy levels 43, 80, 177, 215, 206, 237, 339, 345, and 378 cm^{-1} above the zero-point level. Of these, the 43, 80, 177, 215, 237, and 339 cm^{-1} levels are six of the eight lowest frequency fundamentals in TRA(A) (Table S1 of the Supporting Information).

These low-frequency modes could rise from cross-sequence bands due to Duschinsky rotation induced by the strong mixing. However, another plausible explanation ascribes this emission as a signature of the ^1L_a character of the excited-state level(s) involved, assuming the dominance of vertical emission from the ^1L_a state. On the basis of the calculated Franck−Condon factors, shown pictorially for the absorption spectrum in Figure 5, the ^1L_a origin transition is the most intense band in excitation from the S_0 zero-point level, confirming the near vertical nature of the ^1L_a emission. (The Hessian for the ground state which is required for the calculation of the FC factors was calculated at the B3-LYP/TZVP level and for the excited states at the time-dependent B3-LYP/TZVP level of theory.) The bands in the low-frequency region of Figure 3 should serve as false origins for vibronic structure built off of them, but these are difficult to observe and assign with any certainty because these transitions would be very weak and appear in the midst of the much stronger ^1L_b vibronic bands.

This leads to a model in which the low-frequency emission is a signature of the ^1L_a vibronic character of the mixed excited-state levels giving rise to the emission. By following the position of these bands back toward zero, it is possible to predict the location of the ^1L_a vibrationless level at ∼400−420 cm^{-1} above the ^1L_b origin. The transition at 412 cm^{-1} in the excitation spectrum is the second largest transition in the spectrum. It is the first strong transition with ^1L_a TDM direction. This band also has significant resonance fluorescence which would be consistent with its assignment as the (nominal) ^1L_a origin, which is already in fact a strongly mixed $^1L_a/^1L_b$ level, based on its DF spectra (Figure 4).

The Spectroscopic Consequences of the nearby Conical Intersection. The data on TRA(A) seem to be best understood in terms of a *two-tier* mixing scheme. The excitation spectrum in the 400−600 cm^{-1} region contains several vibronic bands that gain their intensity in excitation from the ^1L_a state. Due to the close proximity of the two states and the conical intersection that connects them, we anticipate coupling spanning large energy separations, which we will refer to as "first tier" coupling.

At the same time, there is significant "second-tier" mixing with near-isoenergetic ^1L_b vibronic levels with coupling matrix elements of 1 cm^{-1} or less. This leads to the presence of multiple transitions within a given band profile. These transitions gain their oscillator strength in excitation from ^1L_a but show the strong ^1L_b character of the excited-state levels in the dominance of ^1L_b emission. Since the number of these contributing transitions closely matches the density of ^1L_b vibrational states, this second-tier mixing between ^1L_a and ^1L_b appears to indiscriminately occur with all ^1L_b vibrational levels in close proximity, breaking down any notion of vibronic selection rules in light of the very small energy separations involved (<1 cm^{-1}).

Higher vibronic levels at 575 and 596 cm^{-1} confirm and strengthen this general picture. The TDM directions and the presence of multiple rotationally resolved transitions indicate that several excited-state levels are involved, all of which gain their oscillator strength (in excitation from the S_0 zero-point level) entirely from the ^1L_a character of the excited-state levels. The nature of the levels involved in the mixing is revealed best in the emission, which is dominated by near-vertical ^1L_b emission, augmented by subtler emission features ascribable to ^1L_a levels not far above the ^1L_a origin.

The transitions that make up the bands at +730 and +913 cm^{-1} have mixed *a/b* character, despite the fact that they are at positions anticipated for strong vibronic bands of ^1L_b. Thus, already by ∼320 cm^{-1} above the ^1L_a "origin", the levels have lost their identity of being ^1L_a and ^1L_b states completely. Taken as a whole, this data set is consistent with the presence of a low-energy conical intersection between the ^1L_b and ^1L_a states in TRA(A). In a strictly adiabatic model it is incorrect to label individual vibronic bands as "^1L_b" or "^1L_a". The adiabatic S_1 PES should exhibit two minima, although DFT/MRCI calculations suggest that the ^1L_a "minimum" is in fact a plateau, from which population can reach the global (^1L_b) minimum via a barrierless process, as shown schematically in Figure 6. At energies well below the CI, the S_1 PES has predominantly ^1L_b character, and both the absorption TDMs and emission spectra are consistent with this simple model. At the energy which first allows the vibronic wave function to extend into the region of configuration space associated with the ^1L_a diabatic minimum, by overcoming the ΔE(elec) and skirting around the CI point in the branching space, ^1L_a character is seen in the absorption of all subsequent bands. First-tier mixing spreads the ^1L_a oscillator strength over several bands, which are then further diluted by second-tier mixing with ^1L_b vibronic levels in near-degeneracy with the strongly coupled levels.

These findings are in close agreement with results on the similar 3-methylindole system by the Callis group. The ^1L_a origin in 3-methylindole is spread over 300 cm^{-1} in a jet spectrum,[63] while they coalesce to a single band approximately 250 cm^{-1} above the ^1L_b origin in an argon matrix. This can be explained by the fact, that the energy gap between ^1L_b and ^1L_a is strongly reduced in the Ar matrix, so that the ^1L_b state density is reduced in the region around the ^1L_a origin. Comparison of the shifts of L_a and L_b upon further methylation in the 2-position in the jet and in an Ar matrix allows assessment of the strength of the first tier coupling to be approximately 100 cm^{-1} and certainly not to exceed 300 cm^{-1}.[3]

Conclusions

The combination of dispersed fluorescence and high-resolution absorption spectroscopy has allowed a uniquely detailed study of the complex interactions occurring between the ^1L_a and ^1L_b states in TRA(A), resulting from Herzberg−Teller coupling and a low-energy conical intersection between these two states.

The onset of the ^1L_a state appears to be around 400 cm^{-1} above the ^1L_b minimum. Vibronic interactions are much stronger than is expected from a mere breakdown of the Condon

approximation. This fact can be traced back to the influence of a nearby conical intersection, which causes a breakdown of the Born−Oppenheimer approximation.

While the general picture proposed seems to account for the observations in a general way, there are aspects of it that still require further refinement. In particular, we do not know with certainty which excited-state levels are primarily responsible for the oscillator strength observed in the excitation scan and what vibronic coupling terms produce them. The DFT-MRCI calculations predict that the $^1L_a \leftarrow S_0$ transition should be seven times more intense than $^1L_b \leftarrow S_0$. However, the ^1L_a character accounts for a surprisingly small fraction of the total emission from all levels probed in this work. Part of this mismatch is accounted for by the first-tier/second-tier mixing scheme which spreads the ^1L_a character of a single ^1L_a level over many ^1L_b levels. Additionally, the integrated intensity of vibronic bands in absorption to the L_a state is about four times larger than for the L_b state as can be inferred from the FC simulations shown in Figure 5. Similarly, the FC factor for emission from L_a levels will approximately be a factor of 4 smaller than from the L_b levels. A different or may be additional explanation for the extremely weak L_a fluorescence might also be found in quenching of the L_a fluorescence via an efficient coupling of a dissociative state (presumably the $\pi\sigma^*$ state) to the L_a state, with only a weak coupling to the L_b state. Nevertheless, the lifetimes of bands belonging to the L_a state are not found to be considerably shorter than the L_b bands.

Calculations that provide accurate predictions for the relative energy and structure of the conical intersection and model the spectroscopy in light of this conical intersection and its coupling to vibronic levels in either state are still needed. Such calculations will shed further light on the role played by traditional HT vibronic coupling versus the derivative coupling characteristic of the conical intersection itself.

Acknowledgment. This work has been performed in the SFB 663 TP A2 (M.S.), A4 (K.K.), and C1 (J.T.), Universität Düsseldorf, with financial support from the Deutsche Forschungsgemeinschaft. We thank Christel Marian for helpful discussions. T.A.L. and T.S.Z. gratefully acknowledge support from the National Science Foundation (CHE-0551075).

Supporting Information Available: Tables of calculated and experimental frequencies of TRA(A) and the Duschinsky submatrix and figures of rotationally resolved spectra and dispersed fluorescence spectra. This material is available free of charge via the Internet at http://pubs.acs.org.

References and Notes

(1) Callis, P. R. L-1(a) and L-1(b) transitions of tryptophan: Applications of theory and experimental observations to fluorescence of proteins. In *Methods in Enzymology*; Brand, L., Johnson, M. L., Eds.; Academic Press: San Diego, CA, 1997; Vol. 278, pp 113−150.
(2) Chen, Y.; Barkley, M. D. *Biochemistry* **1998**, *37*, 9976.
(3) Short, K. W.; Callis, P. R. *Chem. Phys.* **2002**, *283*, 269.
(4) Vivian, J. T.; Callis, P. R *Biophys. J.* **2001**, *80*, 2093.
(5) Bickel, G. A.; Demmer, D. R.; Outhouse, E. A.; Wallace, S. C. *J. Chem. Phys.* **1989**, *91*, 6013.
(6) Callis, P. R. *J. Chem. Phys.* **1991**, *95*, 4230.
(7) Callis, P. R.; Vivian, J. T.; Slater, L. S. *Chem. Phys. Lett.* **1995**, *244*, 53.
(8) Strickland, E. H.; Billups, C. *Biopolymers* **1973**, *12*, 1989.
(9) Strickland, E. H.; Horwitz, J.; Billups, C *Biochem. J.* **1970**, *25*, 4914.
(10) Carney, J. R.; Zwier, T. S. *J. Phys. Chem. A* **2000**, *104*, 8677.
(11) Nguyen, T.; Korter, T.; Pratt, D. *Mol. Phys.* **2005**, *103*, 1603–1613.
(12) Nguyen, T.; Pratt, D. *J. Chem. Phys.* **2006**, *124*, 054317.
(13) Philips, L. A.; Levy, D. H. *J. Chem. Phys.* **1988**, *89*, 85–90.
(14) Philips, L. A.; Webb, S. P.; Martinez, S. J.; Fleming, G. R.; Levy, D. H. *J. Am. Chem. Soc.* **1988**, *110*, 1352.
(15) Schmitt, M.; Böhm, M.; Ratzer, C.; Vu, C.; Kalkman, I.; Meerts, W. L. *J. Am. Chem. Soc.* **2005**, *127*, 10356–10364.
(16) Schmitt, M.; Brause, R.; Marian, C.; Salzmann, S.; Meerts, W. L *J. Chem. Phys.* **2006**, *125*, 124309.
(17) Schmitt, M.; Feng, K.; Böhm, M.; Kleinermanns, K *J. Chem. Phys.* **2006**, *125*, 144303.
(18) Platt, J. R. *J. Chem. Phys.* **1949**, *17*, 484.
(19) Weber, G *Biochem. J.* **1960**, *75*, 335–345.
(20) Sobolewski, A. L.; Domcke, W. *Chem. Phys. Lett.* **1999**, *315*, 293–298.
(21) Dian, B. C.; Longarte, A.; Zwier, T. S. *J. Chem. Phys.* **2003**, *118*, 2696–2706.
(22) Nix, M. G. D.; Devine, A. L.; Cronin, B.; Ashfold, M. N. R. *Phys. Chem. Chem. Phys.* **2006**, *8*, 2610.
(23) Hager, J. W.; Wallace, S. C. *J. Phys. Chem.* **1985**, *89*, 3833.
(24) Sammeth, D. M.; Siewert, S. S.; Spangler, L. H.; Callis, P. R. *Chem. Phys. Lett.* **1992**, *193*, 532.
(25) Borin, A. C.; Serrano-Andrés, L. *Chem. Phys.* **2000**, *262*, 253–265.
(26) Slater, L. S.; Callis, P. R. *J. Phys. Chem.* **1995**, *99*, 8572.
(27) Truhlar, D. G.; Mead, C. *Phys. Rev. A* **2003**, *68*, 2.
(28) Park, Y. D.; Rizzo, T. R.; Peteanu, L. A.; Levy, D. H. *J. Chem. Phys.* **1986**, *84*, 6539–6549.
(29) Wu, Y. R.; Levy, D. H. *J. Chem. Phys.* **1989**, *91*, 5278–5284.
(30) Connell, L. L.; Corcoran, T. C.; Joireman, P. W.; Felker, P. M. *J. Phys. Chem.* **1990**, *94*, 1229–1232.
(31) Caminati, W. *Phys. Chem. Chem. Phys.* **2004**, *6*, 2806–2809.
(32) Clarkson, J. R.; Dian, B. C.; Moriggi, L.; DeFusco, A.; McCarthy, V.; Jordan, K. D.; Zwier, T. S. *J. Chem. Phys.* **2005**, *122*, 214211.
(33) Dian, B. C.; Clarkson, J.; Zwier, T. S. *Science* **2004**, *303*, 1169–1173.
(34) Böhm, M.; Brause, R.; Jacoby, C.; Schmitt, M. *J. Phys. Chem. A* **2009**, *113*, 448–455.
(35) Ahlrichs, R.; Bär, M.; Häser, M.; Horn, H.; Kölmel, C. *Chem. Phys. Lett.* **1989**, *162*, 165–169.
(36) Schäfer, A.; Huber, C.; Ahlrichs, R. *J. Chem. Phys.* **1994**, *100*, 5829–5835.
(37) Stephens, P. J.; Devlin, F. J.; Chabalowski, C. F.; Frisch, M. J. *J. Phys. Chem.* **1994**, *98*, 11623–11627.
(38) Lee, C.; Yang, W.; Parr, R. *Phys. Rev. B* **1988**, *37*, 785–789.
(39) Furche, F.; Ahlrichs, R. *J. Chem. Phys.* **2003**, *117*, 7433.
(40) Ahlrichs, R.; Bär, M.; Baron, H.-P.; Bauernschmitt, R.; Böcker, S.; Deglmann, P.; Ehrig, M.; Eichkorn, K.; Elliott, S.; Furche, F. *TURBOMOLE (version 5.6)*, Universität Karlsruhe, Germany, 2002.
(41) Horn, H.; Weiss, H.; Häser, M.; Ehrig, M.; Ahlrichs, R. *J. Comput. Chem.* **1991**, *12*, 1058.
(42) Deglmann, P.; Furche, F.; Ahlrichs, R. *Chem. Phys. Lett.* **2002**, *362*, 511–518.
(43) Frisch, M. J.; Trucks, G. W.; Schlegel, H. B.; Scuseria, G. E.; Robb, M. A.; Cheeseman, J. R.; Montgomery, J. A., Jr.; Vreven, T.; Kudin, K. N.; Burant, J. C.; Millam, J. M.; Iyengar, S. S.; Tomasi, J.; Barone, V.; Mennucci, B.; Cossi, M.; Scalmani, G.; Rega, N.; Petersson, G. A.; Nakatsuji, H.; Hada, M.; Ehara, M.; Toyota, K.; Fukuda, R.; Hasegawa, J.; Ishida, M.; Nakajima, T.; Honda, Y.; Kitao, O.; Nakai, H.; Klene, M.; Li, X.; Knox, J. E.; Hratchian, H. P.; Cross, J. B.; Adamo, C.; Jaramillo, J.; Gomperts, R.; Stratmann, R. E.; Yazyev, O.; Austin, A. J.; Cammi, R.; Pomelli, C.; Ochterski, J. W.; Ayala, P. Y.; Morokuma, K.; Voth, G. A.; Salvador, P.; Dannenberg, J. J.; Zakrzewski, V. G.; Dapprich, S.; Daniels, A. D.; Strain, M. C.; Farkas, O.; Malick, D. K.; Rabuck, A. D.; Raghavachari, K.; Foresman, J. B.; Ortiz, J. V.; Cui, Q.; Baboul, A. G.; Clifford, S.; Cioslowski, J.; Stefanov, B. B.; Liu, G.; Liashenko, A.; Piskorz, P.; Komaromi, I.; Martin, R. L.; Fox, D. J.; Keith, T.; Al-Laham, M. A.; Peng, C. Y.; Nanayakkara, A.; Challacombe, M.; Gill, P. M. W.; Johnson, B.; Chen, W.; Wong, M. W.; Gonzalez, C.; Pople, J. A. *Gaussian 03, Revision A.1*, Gaussian, Inc., Pittsburgh, PA, 2003.
(44) Bearpark, M. J.; Robb, M. A.; Schlegel, H. B. *Chem. Phys. Lett.* **1994**, *223*, 269–274.
(45) Bernardi, F.; Olivucci, M.; Robb, M. A. *Chem. Soc. Rev* **1996**, *25*, 321–328.
(46) Grimme, S.; Waletzke, M. *J. Chem. Phys.* **1999**, *111*, 5645–5655.
(47) Becke, A. D. *J. Chem. Phys.* **1993**, *98*, 1372–1377.
(48) Schmitt, M.; Küpper, J.; Spangenberg, D.; Westphal, A. *Chem. Phys.* **2000**, *254*, 349–361.
(49) Gerstenkorn, S.; Luc, P. *Atlas du spectre d'absorption de la molécule d'iode 14800−20000 cm^{-1}*; CNRS: Paris, 1986.
(50) Selby, T. M.; Meerts, W. L.; Zwier, T. S. *J. Phys. Chem. A* **2007**, *111*, 3697.
(51) Meerts, W. L.; Schmitt, M.; Groenenboom, G. *Can. J. Chem.* **2004**, *82*, 804–819.
(52) Meerts, W. L.; Schmitt, M. *Phys. Scr.* **2005**, *73*, C47–C52.

(53) Meerts, W. L.; Schmitt, M. *Int. Rev. Phys. Chem.* **2006**, *25*, 353–406.
(54) Berden, G.; Meerts, W. L.; Jalviste, E. *J. Chem. Phys.* **1995**, *103*, 9596–9606.
(55) Varsanyi, G. *Assignments for Vibrational Spectra of 700 Benzene Derivatives*; Wiley: New York, 1974.
(56) Roth, W.; Jacoby, C.; Westphal, A.; Schmitt, M. *J. Phys. Chem. A* **1998**, *102*, 3048–3059.
(57) Doktorov, E. V.; Malkin, I. A.; Man'ko, V. I. *J. Mol. Spectrosc.* **1977**, *64*, 302–326.
(58) Duschinsky, F. *Acta Physicochim. U.R.S.S.* **1937**, *7*, 551.
(59) Dedonder-Lardeux, C.; Jouvet, C.; Perun, S.; Sobolewski, A. *Phys. Chem. Chem. Phys.* **2003**, *5*, 5118.
(60) Smolyar, A.; Wong, C. F. *J. Mol. Struct.: THEOCHEM* **1999**, *488*, 51–67.
(61) Fender, B. J.; Sammeth, D. M.; Callis, P. R. *Chem. Phys. Lett.* **1995**, *239*, 31.
(62) Barstis, T. L. O.; Grace, L. I.; Dunn, T. M.; Lubman, D. L. *J. Phys. Chem.* **1993**, *97*, 5820.
(63) Fender, B.; Callis, P. R. *Chem. Phys. Lett.* **1996**, *262*, 343–348.

JP810502V